PCCP

ROYAL SOCIETY OF CHEMISTRY

PAPER

View Article Online
View Journal

Cite this: DOI: 10.1039/d6cp00757k

DFT insights into optoelectronic properties of a 1 : 1 perylene : TCNQ cocrystal as a near-infrared absorber for photovoltaic applications

Arkalekha Mandal, *[a] Chris Erik Mohn,[a] Yusuf Chanchangi[b] and Carl Henrik Görbitz[a]

With the advent of lightweight photovoltaic materials with room-temperature solution processing ability, organic materials have emerged as a particularly promising family of candidates. Organic cocrystals comprising π-electron-rich donors and π-electron-deficient acceptors show immense potential within the field of thin film photovoltaic devices, possessing strong and broad optical absorption covering the visible and near-infrared region of the solar spectrum, intrinsic semiconductor properties, and solution-processing ability under ambient conditions. However, they have been scarcely studied as materials for photovoltaic devices. Herein, we investigated the excited-state features and electron/hole transport properties of a 1 : 1 cocrystal of π-donor perylene and π-acceptor 7,7′,8,8′-tetracyanoquinodimethane (TCNQ). The donor and acceptor molecules form infinite π-stacks *via* strong face-to-face π···π stacking interactions to facilitate charge transfer. The absorption spectrum of this cocrystal shows quite broad absorption from the UV to the near infrared regions (320–1150 nm) owing to charge transfer. The time-dependent DFT study indicates efficient charge transfer and exciton generation and dissociation. The bandgap (0.92 eV) and the exciton binding energy (0.12 eV) values of this cocrystal are ideal for photovoltaic applications, while its theoretically calculated spectroscopic limited maximal efficiency (SLME) is 24% at 1000 nm thickness, indicating its future applicability. The electron (45 meV) and hole (48 meV) transfer integral values along the π···π stacking direction indicate ambipolar charge transport, while the low internal reorganization energy values of perylene (147 meV) and TCNQ (255 meV) are favourable for fast charge carrier transport, making the cocrystal a suitable candidate for photovoltaic applications. The 1 : 1 perylene : TCNQ cocrystal represents an intriguing example of an indirect bandgap organic material with a high theoretical maximum photovoltaic efficiency at low film thickness owing to the very similar values of its indirect bandgap and direct allowed bandgap. This theoretical study unveils the photophysical and charge transport properties of an organic cocrystal with strong potential for photovoltaic applications.

Received 28th February 2026,
Accepted 17th April 2026

DOI: 10.1039/d6cp00757k

rsc.li/pccp

Introduction

In the last two decades, organic molecular crystals have been recognised as potential photovoltaic materials.[1,2] Rubrene-,[3] pentacene-,[4] and fullerene-based[5] molecular crystals have been explored as organic photovoltaic materials as they exhibit strong photon absorption and excellent charge carrier mobility values. However, these materials are known for their limited solubility, and hence, fabricating good-quality thin films of these materials is often challenging.[6] Recently, a number of non-fullerene small molecules have emerged as acceptors for bilayer or bulk heterojunction solar cells.[7–11] The addition of alkyl substituents in the molecular backbones helps to overcome the solubility issue in these non-fullerene acceptors. On the other hand, the fabrication of heterojunction solar cells is more complicated, and the poor donor–acceptor interface morphology often reduces the overall photo-conversion efficiency due to charge trapping.[12,13] In this regard, organic ambipolar molecular crystals can be suitable candidates as the integration of both p-type and n-type semiconductor behaviour in a single material and minimal charge traps in their crystalline domains will facilitate good photovoltaic properties.[14,15]

Ambipolar semiconductor properties are very rare in organic semiconductors as the majority of organic molecular semiconductors are p-type,[16–18] while few molecular semiconductors

[a] Department of Chemistry, Blindern Campus, University of Oslo, Oslo 0371, Norway. E-mail: arkalekha.mandal@kjemi.uio.no, arkalekhamandal@gmail.com
[b] Environmental and Sustainability Institute, Faculty of Environment, Science and Economy, University of Exeter, Exeter, Penryn Campus, Cornwall TR10 9FE, UK

are n-type in nature.[19,20] A promising attempt to realize ambipolar semiconductor properties in organic systems was achieved by assembling π-donor and π-acceptor moieties in a single-component structure *via* polymerization[21,22] or cocrystallization.[23] Cocrystallization of π-donor (D) and π-acceptor (A) molecules is the most viable and the least tedious method for obtaining ambipolar organic semiconductors with good solution processing ability.[23–27] Ambipolar organic donor–acceptor cocrystals with bandgaps in the range of 1.0 to 1.8 eV, strong photon absorption in the visible and near-infrared region of solar spectrum, facile exciton generation and dissociation ability, and balanced electron and hole transport will be the attractive choices as thin-film organic photovoltaic materials.[28,29]

In the present work, we explored the electronic and charge carrier transport properties of a 1 : 1 donor–acceptor cocrystal composed of a perylene donor and 7,7′,8,8′-tetracyanoquinodimethane (TCNQ) acceptor in both ground and optically excited states (Scheme 1). Perylene is a well-known polycyclic aromatic hydrocarbon (PAH) donor component of numerous organic cocrystals with remarkable semiconductor[30,31] and fluorescent[32–34] properties. Alternatively, the π-acceptor TCNQ is a widely used molecule to impart n-type and ambipolar semiconductor properties in both organic cocrystals[35–37] and metal organic frameworks.[38,39] Cocrystallization of perylene and TCNQ to produce 1 : 1, 3 : 1 and 3 : 2 cocrystals has been reported.[40,41] The charge carrier transport properties of the 1 : 1 perylene : TCNQ cocrystal have been studied experimentally *via* the fabrication of a field-effect transistor, and electron mobility values in the range of 0.001–0.01 $cm^2\ V^{-1}\ s^{-1}$ have been reported.[41] However, the excited-state and photovoltaic properties of the 1 : 1 perylene : TCNQ cocrystal have not been explored thus far. The complementarity of the molecular electrostatic potential (MEP) of perylene and TCNQ indicates efficient π···π stacking interactions (Fig. 1a). In addition, the small energy difference (∼0.14 eV) between the perylene HOMO and the TCNQ LUMO (Fig. 1b) will lead to efficient charge transfer. We envisage that the 1 : 1 perylene : TCNQ cocrystal possesses excellent photovoltaic properties owing to both the strong face-to-face π···π stacking between perylene and TCNQ and facile charge transfer suitable for absorption in the red and near-infrared regions of the solar spectrum.

It is known that charge transfer leads to efficient absorption in the visible and near-infrared regions for facile exciton generation, and this, together with the already reported charge carrier transport properties of the 1 : 1 perylene : TCNQ cocrystal, is conducive to photovoltaic applications. In the current work, we investigate the excited-state and ambipolar charge transport properties of a 1 : 1 perylene : TCNQ cocrystal to demonstrate its potential as a photovoltaic material.

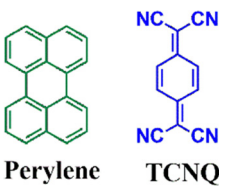

Scheme 1 Donor and acceptor molecules in the studied 1 : 1 cocrystal.

Materials and methods

Synthesis of 1 : 1 perylene : TCNQ cocrystal

The 1 : 1 perylene : TCNQ cocrystal (literature reported, CCDC number: 1576698) was synthesized by grinding an equimolar amount of perylene (50 mg, 2 mmol) and TCNQ (40 mg, 2 mmol) with the repetitive addition of 0.5 mL of toluene at 5-min intervals. The resultant dark green powder was dissolved in 5 mL of chlorobenzene and left undisturbed at room temperature for slow evaporation. Long prismatic blackish green crystals grew after one week (Fig. S2, SI). Mechanochemical cocrystal synthesis was employed as a green chemistry approach.

Spectroscopic characterization

Single crystals of 1 : 1 perylene : TCNQ cocrystal (50 mg) were collected and dissolved in 10 mL of chlorobenzene. Solid polymethylmethacrylate (PMMA) polymer (50 mg) was dissolved in 10 mL chlorobenzene at 50 °C. The cocrystal solution was poured into the PMMA solution, and the mixed solution was stirred for a few minutes. The mixed solution was then drop-cast on glass slides and annealed at 60 °C to prepare yellow coloured drop-cast thin films. A PerkinElmer LAMBDA 1050+ UV/Vis/NIR spectrophotometer was employed to record

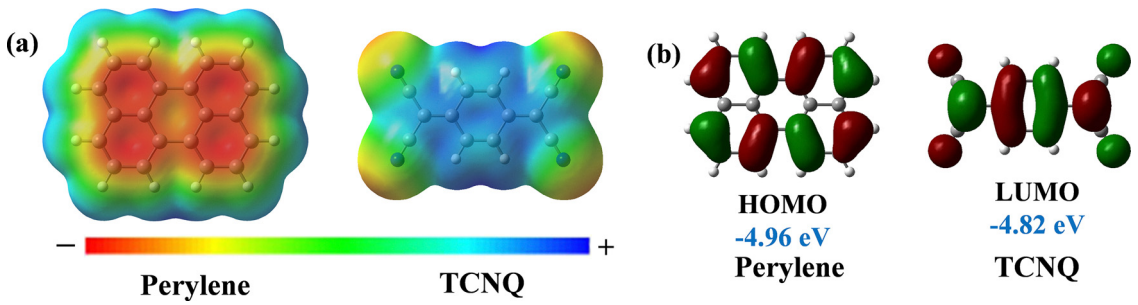

Fig. 1 (a) Molecular electrostatic potentials of perylene and TCNQ calculated at the B3LYP/6-31G(d,p) level in the gas phase and (b) energies of HOMO of perylene and LUMO of TCNQ calculated at the B3LYP/6-31G(d,p) level of theory on optimized gas phase geometries.

absorbance and transmittance data. The instrument was operated in absorbance mode, with the data recorded at 5-nm intervals across a wavelength range from 300 to 1800 nm, encompassing the ultraviolet (UV), visible (Vis), and near-infrared (NIR) regions. The optical bandgap of the cocrystal was determined from its Tauc plot, which is widely used for the evaluation of amorphous (powder) or disordered (solution-processed thin film) materials. The photon energy ($h\nu$) is plotted along the x-axis, while the quantity $(\alpha h\nu)^{1/2}$ (for indirect bandgap) or $(\alpha h\nu)^2$ (for direct bandgap) is plotted along the y-axis, with α being the absorption coefficient of the material. Extrapolation of the curve along the abscissa produces the optical bandgap energy of a semiconductor material.

Computational methods

Theoretical estimation of intermolecular interaction energies

The binding energies between the π-stacked or weak hydrogen-bonded donor and acceptor moieties in the gas-phase dimer were calculated at the crystal geometry (literature reported, CCDC number: 1576698) using Grimme's dispersion with the Becke–Johnson damping-corrected B3LYP functional (B3LYP-D3-BJ) and 6-31G(d,p) basis set. The counterpoise method was used to correct the basis set superposition error (BSSE) as we used a relatively small basis set for calculating the intermolecular interaction energy.[42] The binding energy values corresponding to π···π stacking and hydrogen-bonding interactions in the solid state were calculated at the B3LYP/6-31G(d,p) level of theory using CrystalExplorer.[43,44]

Theoretical prediction of optoelectronic properties at the molecular level

The Gaussian 16 program package was used for all calculations at the atomic level. The HOMO/LUMO energies and molecular electrostatic potential surfaces of the donor and acceptor molecules were calculated at the B3LYP/6-31G(d,p) level of theory. The HOMO/LUMO energies of the D–A dimer, A–D–A–D tetramer, and A–D–A–D–A–D hexamer were calculated using Grimme's dispersion (D3)[45] corrected B3LYP functional with the 6-31G(d,p) basis set, using the atomic coordinates extracted from the room temperature crystal geometry reported in the literature. The Becke–Johnson damping function was used, along with the dispersion-corrected D3 functional.[46] The donor-to-acceptor charge transfer was quantified from the natural bond orbital (NBO)[47] analysis of the π-stacked perylene–TCNQ dimer using Grimme's dispersion (D3)-corrected B3LYP functional. The second-order perturbation (E^2) energy[48] values for electron transfer from the filled π-orbitals on perylene to the empty π*-orbitals on TCNQ, along with the NBO atomic charges on these moieties give an estimation of charge transfer from perylene to TCNQ.

To calculate the excited-state properties, time-dependent DFT (TD-DFT) calculations were performed on the D–A dimer and A–D–A–D tetramer using the experimental coordinates from the crystal structure reported in the literature. The CAM-B3LYP functional[49,50] was used for the TD-DFT calculations, and only spin-allowed singlet–singlet transitions were considered for the optically excited states. The CAM-B3LYP range-separated exchange–correlation functional, with 19% Hartree–Fock exchange at short range, 65% Hartree–Fock exchange at long range (>10 Å), and 33% HF (HF) exchange in the intermediate range, takes into account the long-range electron–electron coupling effect in π-stacked D–A systems to produce reliable transition energy values. The electron–hole distribution, coefficient of electron–hole mixing,[51] charge transfer length,[52] and one-electron transition density matrix[52] for the excited states were obtained from the TD-DFT calculation results. The Multiwfn software[51,52] was used to plot the excited-state electron–hole distribution maps and heat maps for the one-electron transition density matrix,[53] and calculating the charge transfer lengths and electron–hole mixing coefficient. Another range-separated hybrid functional, ωB97X-D, was used to calculate the excited-state properties of the π-stacked D–A dimer and A–D–A–D tetramer, and the values of different parameters were compared with those obtained using the CAM-B3LYP functional. The range-separated ωB97X-D functional is comprised of 22% Hartree Fock exchange at short range and 100% Hartree Fock exchange at long range, while the intermediate region is defined with a standard error function with a range separation parameter value of 20%.[54]

Modelling of charge carrier transfer

The internal hole/electron reorganization energy (λ_{int}) of the donor and acceptor molecules was calculated at the B3LYP/6-31G(d,p) level by adding the molecular reorganization energy at both the neutral ground (λ_i) and charged excited (λ_f) states upon molecular cation/anion formation. A four-point energy model[55] was employed to estimate the internal reorganization energy (λ_{int}) of the molecules, as follows:

$$\lambda = \lambda_i + \lambda_f = \left(E^{**}_{cation/anion} - E_{neutral}\right) + \left(E^{*}_{cation/anion} - E_{cation/anion}\right), \quad (1)$$

$$\lambda_i = \left(E^{**}_{cation/anion} - E_{neutral}\right), \text{ and } \lambda_f = \left(E^{*}_{cation/anion} - E_{cation/anion}\right)$$

where $E_{neutral}$ and $E_{cation/anion}$ represent the energies of the optimized geometry of the neutral molecule and optimized geometry of the cation/anion, respectively. Alternatively, $E^{*}_{cation/anion}$ and $E^{*}_{cation/anion}$ refer to the single-point energy of the cation/anion with the optimized geometry of the neutral state of molecule and the single-point energy of the neutral molecule with the optimized geometry of the cationic/anionic states, respectively.

The super-exchange and direct electron and hole transfer integrals were calculated at the CAM-B3LYP/6-31G(d,p) level of theory. The long-range-corrected CAM-B3LYP functional was used for the transfer integral calculation as the frontier molecular orbitals in the non-covalently bonded molecular dimers (D–D/A–A) or π-stacked trimers (A–D–A/D–A–D) are generally distributed on two different molecules. Hence, transfer integral calculations necessitate the long-range electron correlation for

calculating the energy of molecular orbitals distributed on multiple molecules.

Band structure calculations

Band structure calculations for the perylene:TCNQ cocrystal were performed using both the reported room-temperature (290 K) experimental and optimized unit cell geometries in the Vienna *ab initio* Simulation package (VASP, version 6.4.3). Geometry optimization was performed with the van der Waals density functional (vdW-DF) with an energy cut-off of 700 eV and a convergence criterion of 10^{-7} eV Å^{-1}. A Γ-centered $4 \times 3 \times 2$ k-point mesh and Gaussian smearing with a smearing width of 0.03 eV were used to optimize the unit cell volume, shape, and basic atomic positions. The van der Waals density functional was used for optimization as the crystal packing of the cocrystal is dominated by van der Waals-type π···π and C–H···π interactions. The unit cell parameters from the experimental and optimized geometries are as follows; experimental: a = 7.30 Å, b = 10.87 Å, c = 14.55 Å; optimized with vdW-DF: a = 7.50 Å, b = 10.90 Å, c = 14.52 Å.

Band structure calculations on the experimental and DFT optimized geometries were performed with an energy cut-off of 500 eV and a Monkhorst–pack k-point mesh of $5 \times 3 \times 2$ for the SCF total energy calculation and a k-point density of 0.06 Å^{-1} between the high-symmetry points to draw the band structure. A convergence criterion of 10^{-7} eV Å^{-1} for the electronic wavefunction was applied to calculate the band structure using the HSE06 hybrid DFT functional. The HSE06 functional has been recognized to give an accurate band structure value for organic systems.[56,57] A Gaussian smearing scheme with a smearing width of 0.02 eV was used for band structure calculations. The band structure calculation for the 1-aminopyrene:TCNQ cocrystal (CCDC: 1915543) was performed using the experimental geometry and the HSE06 functional, while geometry optimization was performed for the CBP:$(TCNQ)_2$ (CBP = π-donor 4,4′-bis-(carbazol-9-yl)biphenyl) cocrystal (CCDC: 2058993). The C17, C18, H17, and H18 atoms of the CBP:$(TCNQ)_2$ cocrystal have 80 : 20 occupancies distributed over two positions. We considered full occupancies at the atomic sites with an experimental 80% occupancy and removed atomic sites with a 20% occupancy manually to carry out the geometry optimization. The van der Waals density functional (vdW-DF) was employed with an energy cut-off of 600 eV, a Γ-centered $2 \times 2 \times 1$ mesh of k-points, and a convergence criterion 10^{-7} eV Å^{-1} for optimizing the basic atomic positions while keeping the unit cell geometry fixed.

The VASPKIT software (version 1.3.5) was used for post processing of all the data including calculation of the spectroscopy limited maximum efficiency (SLME) parameter required for photoconversion property evaluation. The SLME parameter η value is calculated as $\eta = P_m/P_{in}$, where P_m is the maximum power density obtained from the material and P_{in} is the incident power density from the solar spectrum. The η value is extracted using an exponential function to model the fraction of radiative recombination, as stated in the following equation:

$$J_{SC} = J_0 \exp \int_0^{\infty} a(E) I_{sun} E \mathrm{d}E; \quad (2)$$

where J_{SC} is the photovoltaic current, $a(E)$ is photon absorptivity, I_{sun} is AM 1.5 G solar spectrum (wavelength range 280–2000 nm), and J_0 is the reverse photocurrent, which depends on both radiative and non-radiative recombination in the dark state and is determined using the following expression:

$$J_0 = J_0^{r} + J_0^{nr} = J_0^{r}/\exp(E_g - E_g^{da}/kT); \quad (3)$$

where E_g is the fundamental bandgap and E_g^{da} is the direct allowed bandgap. Consequently, the SLME value tends to zero for indirect bandgap materials if difference between the direct allowed and fundamental bandgap becomes large. In contrast, the SLME parameter gives a fairly comprehensive idea of the theoretical maximum photoconversion efficiency for direct bandgap materials, and also for indirect bandgap materials with considerably small differences between their indirect bandgap and direct allowed bandgap. The SLME parameter gives a more practical estimate of efficiency than the traditional Shockley–Queisser (SQ) limit, which only takes into account radiative charge carrier recombination.[58] In contrast, the SLME parameter accounts for both radiative and non-radiative recombination, providing comprehensive insights into the photoconversion efficiency.

Results and discussion

Crystal packing of 1 : 1 perylene TCNQ cocrystal

The 1 : 1 perylene : TCNQ cocrystal (Fig. S1, SI) is crystallized in the centrosymmetric monoclinic space group $P2_1/c$. Its asymmetric unit contains a half-molecule of perylene and half-molecule of TCNQ, and two of these asymmetric units are present in its unit cell. The perylene and TCNQ molecules are tethered in an infinite chain along the crystallographic a axis *via* strong face to face π···π stacking interactions. The distance between the centroids (C_g) of the 20-member aromatic core of perylene and the 6-membered quinonoid core of TCNQ is 3.469 Å, while the angle between these planes is 4.40° (Fig. 2a). The infinite ···D–A–D–A··· molecular stacks present in the crystal packing (Fig. 2b and Table 1) are adjoined by a C9–H9···N1 (C···N, 3.431(2) Å; C···N, 2.71 Å, and C–H···N, 134.8°) hydrogen bond along the crystallographic c axis, and by a C7–H7···N2 (C···N, 3.523(3) Å; C···N, 2.67 Å, and C–H···N, 153.3°) hydrogen bond along the crystallographic b axis (Fig. 2c and Table 1).

The strength of the intermolecular interactions was estimated both in the gaseous and solid phase using the experimentally observed coordinates of the molecular dimers. The binding energy of the face to face π···π stacking interactions in the gas phase and solid state is −21.98 and −15.02 kcal mol^{-1}, respectively. The strength of the C–H···N hydrogen bonds in the gas phase is −1.58 and −2.19 kcal mol^{-1}, which is significantly less than the strength of the π···π stacking interactions. This indicates that π···π stacking is the major attractive non-covalent interaction in the crystal packing and points to the direction of charge carrier transport.

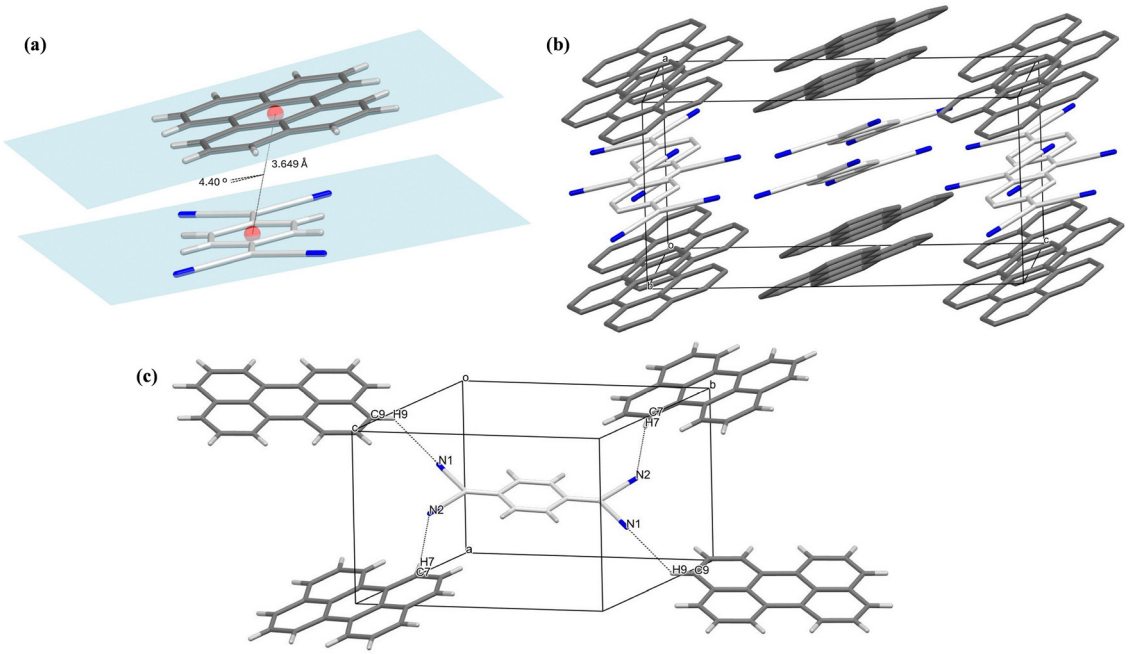

Fig. 2 (a) Parameters of face-to-face π···π stacking between the donor and acceptor; (b) molecular stacks formed by alternating perylene and TCNQ molecules; and (c) C–H···N hydrogen boding interactions between the perylene and TCNQ molecules from different π-stacks leading to three dimensional crystal packing, the carbon atoms of the perylene and TCNQ molecules are coloured differently for visualization.

Table 1 Non-covalent interaction parameters observed in crystal packing of the 1 : 1 perylene : TCNQ cocrystal

Interaction	D···A (Å)	H···A (Å)	D–H···A (°)	Symmetry
π···π stacking	3.469			x, y, z
C9–H9···N1	3.431(2)	2.71	134.8	$1-x, 1-y, 1-z$
C7–H7···N2	3.523(3)	2.67	153.3	x, y, z

Ground-state electronic properties of the 1 : 1 perylene : TCNQ cocrystal

The frontier molecular orbital analyses of the perylene : TCNQ cocrystal were carried out using both the B3LYP functional with the Grimme's D3 dispersion correction and Becke–Johnson damping factor (B3LYP-D3-BJ) and the range-separated CAM-B3LYP functional. The HOMO–LUMO difference is 1.68 eV with the B3LYP functional including D3-BJ dispersion correction, whereas it is 3.3 eV with the CAM-B3LYP functional. In contrast, the geometrical offset of the molecular orbitals is unchanged with the use of DFT-functionals as the HOMO is concentrated on the perylene and the LUMO is located on TCNQ (Fig. 3 and Fig. S3 in the SI). The HOMO−1 orbital is observed to be primarily located on the acceptor, while the HOMO−2 orbital is based on the donor. The LUMO+1 orbital is observed to be fully concentrated on the perylene molecule by CAM-B3LYP calculation (Fig. S3, SI), while the application of the B3LYP functional with D3-BJ dispersion produces the LUMO+1 orbital mainly located on the TCNQ molecule (Fig. 3). The frontier molecular orbitals of the D–A–D–A tetramer were analyzed at the B3LYP-D3-BJ/6-31G(d,p) level of theory (Fig. S4 and S5) using both the CAM-B3LYP functional and the B3LYP functional with Grimme's D3 dispersion correction. Similar geometrical offsets of the HOMO and LUMO were observed, with a HOMO/LUMO gap of 1.23 eV obtained using the B3LYP-D3 functional. In contrast, the HOMO/LUMO gap in the π-stacked hexameric D–A–D–A–D–A unit calculated at the B3LYP-D3/6-31G(d,p) level of theory is 1.38 eV (Fig. S6, SI).

The donor-to-acceptor charge transfer was confirmed by natural bond orbital (NBO) analysis, with significant values obtained for the second-order perturbation energy E^2 (Fig. 4). We also calculated the degree of ground-state charge transfer

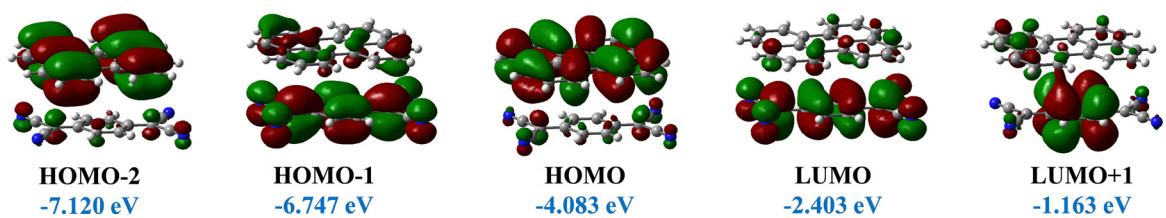

Fig. 3 Frontier molecular orbitals of D–A dimer calculated at the B3LYP-D3-BJ/6-31G(d,p) level.

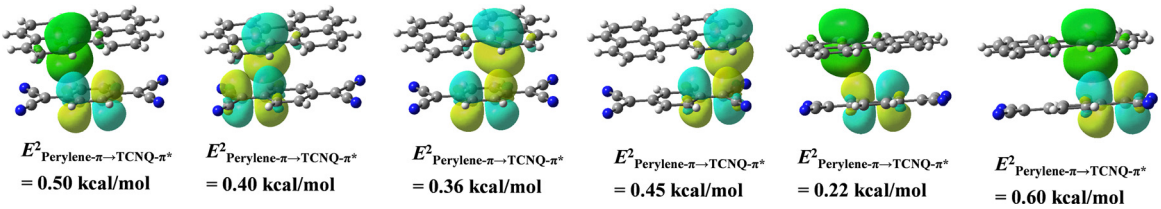

Fig. 4 Natural bond orbital analysis on the π-stacked D–A dimer, where the second-order perturbation energy E^2 values indicate significant charge transfer.

using the NBO method as NBO charges are considered to be more accurate than Mulliken charge analysis. The degree of ground-state charge transfer is around 0.2, indicating the prominent CT character of the 1 : 1 perylene : TCNQ cocrystal. This degree of charge transfer from our study matches closely with that reported in the literature.[41a]

Optical and excited-state properties of the 1 : 1 perylene : TCNQ cocrystal

The absorption spectrum of the 1 : 1 perylene : TCNQ cocrystal was recorded in the range of 300–1500 nm using drop-cast thin-film samples. A broad charge-transfer absorption band is observed, spanning from the red end of the visible region to the near-infrared region (600–1150 nm). More well-defined and intense absorption peaks (325–550 nm) are observed in the UV and blue-green regions of the visible spectrum (Fig. 5).

We carried out a time-dependent DFT study on the π-stacked D–A dimer and D–A–D–A tetramer using two range-separated and long-range-corrected DFT functionals, CAM-B3LYP and ω97X-D, with 33% and 20% Hartree Fock exchange at the short range, respectively. The TD-DFT results obtained using the CAM-B3LYP functional on the D–A dimer show that the $S_0 \rightarrow S_1$ (815 nm, oscillator strength = 0.072) and $S_0 \rightarrow S_3$ (389 nm, oscillator strength = 0.023) transitions (Fig. 6 and Table 2) have predominant charge transfer nature. In contrast, the $S_0 \rightarrow S_2$ (422 nm, oscillator strength = 0.126) mainly originates from the intramolecular excitation in the TCNQ molecule.

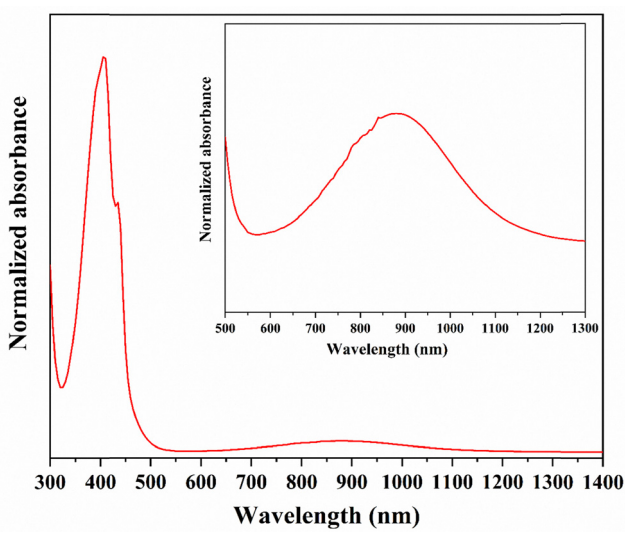

Fig. 5 Absorption spectrum of the 1 : 1 perylene : TCNQ cocrystal drop-cast thin-film samples, with the near-infra-red region shown in the inset figure.

The charge transfer character of the excited-state electron–hole pair was further analyzed (Fig. 7a). The electron–hole mixing parameter for the excited S_1 and S_3 states is 0.38 and 0.42, respectively, indicating the substantial charge transfer character of these excite states. The charge transfer length, *i.e.*, the length of the electron and hole epicenters in the S_1 and S_3 states, is 3.38 and 2.81 Å, respectively (Table 4). Alternatively, the S_2 state (422 nm, oscillator strength = 0.126) has very prominent local excitation character, as confirmed by the electron–hole mixing coefficient of 0.49 and the charge transfer length of 0.84 Å (Table 4). We performed electron transition density matrix analysis for $S_0 \rightarrow S_1$, $S_0 \rightarrow S_2$ and $S_0 \rightarrow S_3$; the heat maps of the transition density matrix for the $S_0 \rightarrow S_1$ and $S_0 \rightarrow S_3$ transitions show bright off-diagonal elements, confirming the charge transfer character (Fig. 7b). The large and very bright off-diagonal elements for the $S_0 \rightarrow S_1$ transition indicates exclusive charge transfer origin. In contrast, the heat map of the electron transition density matrix of the $S_0 \rightarrow S_2$ transition shows bright diagonal elements, indicating local excitation nature (Fig. 7b). Similar results were obtained using the ω97X-D functional (Table S2 and Fig. S7 in SI), further confirming the charge transfer character of the $S_0 \rightarrow S_1$ and $S_0 \rightarrow S_3$ transitions and local excitation nature of the $S_0 \rightarrow S_2$ transition.

A time-dependent analysis was also performed for the π-stacked D–A–D–A tetramer to check the convergence of the calculation results obtained from the D–A dimer. The TD-DFT analysis carried out on the tetramer confirms the prominent charge transfer character of $S_0 \rightarrow S_1$ (1.60 nm, oscillator strength = 0.202) and $S_0 \rightarrow S_3$ (640 nm, oscillator strength = 0.037), while $S_0 \rightarrow S_2$ (750 nm), $S_0 \rightarrow S_4$ (540 nm) are dark transitions with zero oscillator strength (Table 3 and Fig. 8). In contrast, the $S_0 \rightarrow S_5$ (432 nm, oscillator strength = 0.046) and $S_0 \rightarrow S_6$ (420 nm, oscillator strength = 0.132) transitions have prominent local excitation character due to intramolecular transitions in TCNQ (Fig. 8). We carried out the excited-state and one-electron transition density matrix analyses to further confirm the generation of charge transfer excitations upon light absorption. The electron–hole distribution analyses for the S_1 and S_3 excited states show prominent geometrical offset with the holes concentrated on the donor and the electrons

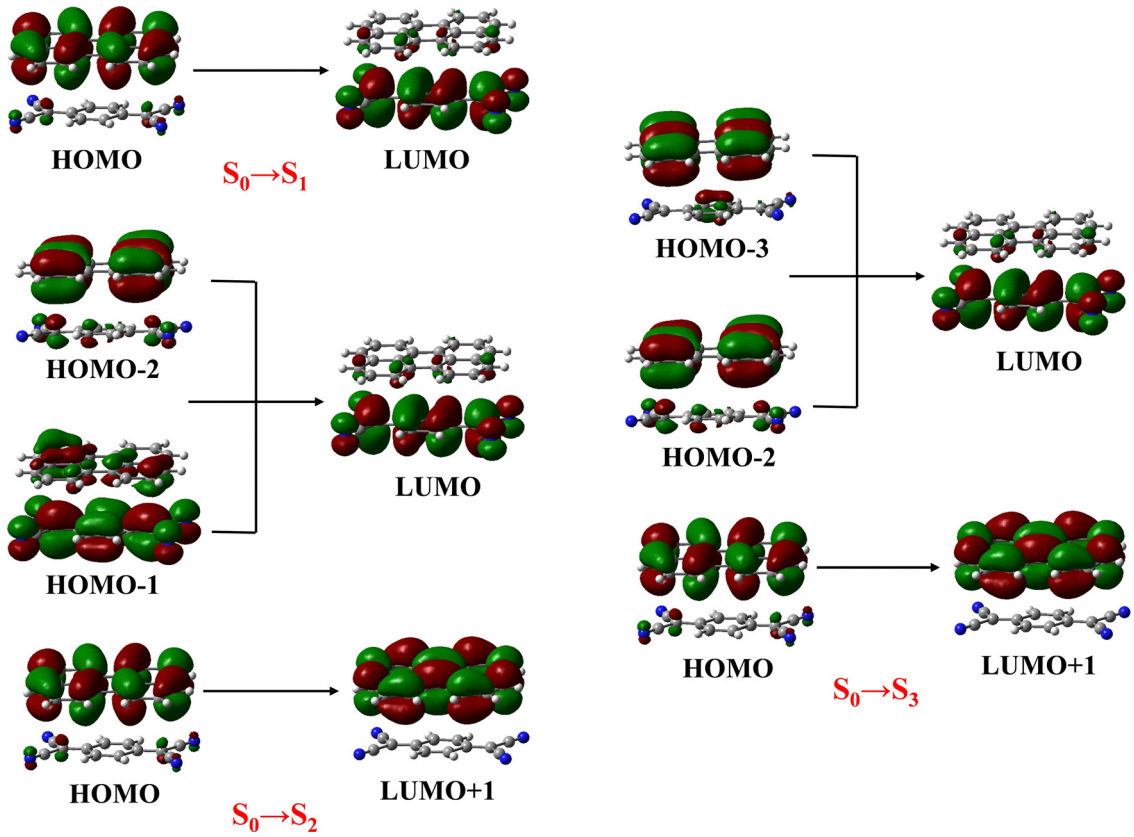

Fig. 6 Molecular orbitals taking part in the $S_0 \rightarrow S_1$, $S_0 \rightarrow S_2$ and $S_0 \rightarrow S_3$ transitions of π-stacked D–A dimer, where the time-dependent DFT analysis was carried out at the CAM-B3LYP/6-31G(d,p) level.

Table 2 Calculated wavelength, transition energy, oscillator strength and orbital contributions for the $S_0 \rightarrow S_1$, $S_0 \rightarrow S_2$ and $S_0 \rightarrow S_3$ transitions in the D–A dimer at the CAM-B3LYP/6-31G(d,p) level

Transition	Wavelength (nm)	Energy (eV)	Oscillator strength	Orbital contribution
$S_0 \rightarrow S_1$	815	1.52	0.0723	HOMO → LUMO, 100%
$S_0 \rightarrow S_2$	422	2.94	0.1260	HOMO−2 → LUMO, 2.19%
				HOMO−1 → LUMO, 72.83%
				HOMO → LUMO+1, 24.98%
$S_0 \rightarrow S_3$	389	3.18	0.0228	HOMO−3 → LUMO, 16.65%
				HOMO−2 → LUMO, 67.73%
				HOMO → LUMO+1, 15.62%

primarily located on the acceptor (Fig. 9a); however, considerable electron–hole mixing is observed for the S_5 and S_6 states (Fig. 9a). The degree of electron–hole mixing for the excited S_1, S_3, S_5, and S_6 states is 0.34, 0.37, 0.82 and 0.73, respectively, indicating the prominent local excitation character of the S_5 and S_6 states. The charge transfer length, *i.e.*, a rough estimate of the exciton size corresponding to the S_1 and S_3 states, is 7.67 and 6.46 Å, respectively, which confers the possibility of plausible charge-transfer excitation dissociation (Table 4).[59] In contrast, the charge transfer lengths for the locally excited S_5 and S_6 states are 0.93 and 3.28 Å, respectively (Table 4), which are unfavourable for exciton dissociation.[59,60] The heat maps of the one-electron transition density matrix for the $S_0 \rightarrow S_1$ and $S_0 \rightarrow S_3$ transitions demonstrate bright off-diagonal elements but no diagonal elements, confirming their pure charge transfer origin (Fig. 9b). Alternatively, the $S_0 \rightarrow S_5$ and $S_0 \rightarrow S_6$ transitions are characterized with only diagonal elements, which indicate their local excitation origin.

Charge carrier transport in 1 : 1 perylene : TCNQ cocrystal

Electron and hole transport in molecular semiconductors occurs *via* the hopping mechanism. The rate of charge carrier transport, k_T, *via* the hopping mechanism can be expressed as the Marcus–Hush equation, as follows:[61]

$$(k_T):k_T = \frac{4\pi^2}{h}\frac{1}{\sqrt{4\pi\lambda k_B T}}t^2 \exp\left[\frac{-(\Delta G^\circ + \lambda)^2}{4k_B\lambda T}\right]. \quad (4)$$

where t, λ, and ΔG° denote transfer integral, reorganization energy, and free energy of electron transfer, respectively.

Charge carrier transport in mixed-stack D–A cocrystals can occur *via* both super-exchange and direct pathways. An electron (or a hole) is transported from the LUMO of one acceptor (or the HOMO of one donor) molecule to the LUMO of a neighbouring acceptor (or the HOMO of the next donor) molecule *via* the HOMO of a bridging donor (or the LUMO of a bridging acceptor) molecule. The super-exchange electron transfer integral is calculated from the energy splitting between the LUMO orbitals (*i.e.*, LUMO and LUMO+1) of the π-stacked A–D–A molecular trimer, while the super-exchange hole transfer

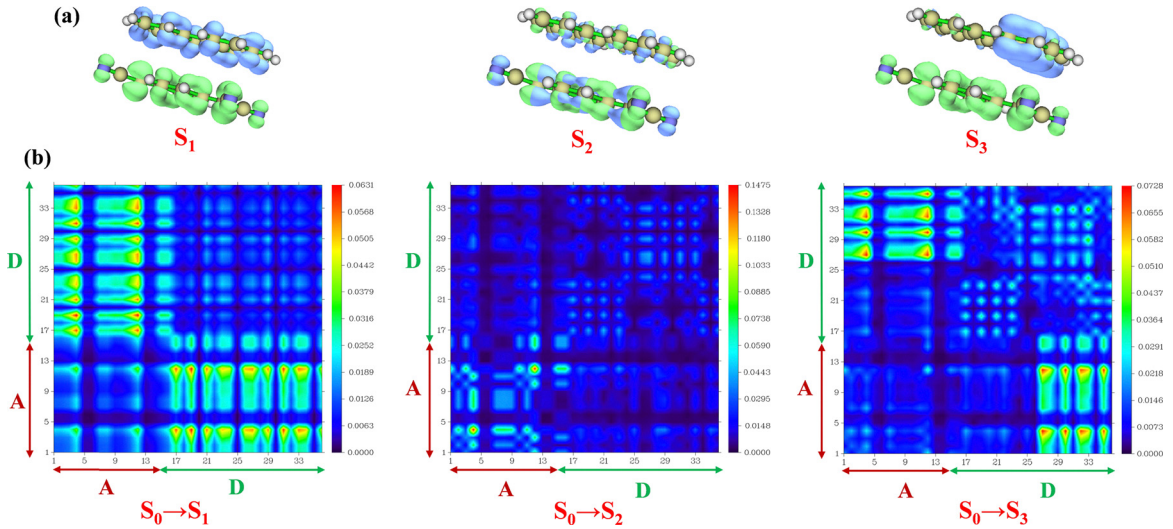

Fig. 7 (a) Electron–hole distribution maps in excited states S_1, S_2 and S_3 calculated at the CAM-B3LYP/6-31G(d,p) level of theory on the π-stacked D–A dimer and (b) heat maps of one-electron transition density matrix for $S_0 \rightarrow S_1$, $S_0 \rightarrow S_2$ and $S_0 \rightarrow S_3$ transitions of the π-stacked D–A dimer.

Table 3 Calculated wavelength, transition energy, oscillator strength and orbital contributions for the $S_0 \rightarrow S_1$, $S_0 \rightarrow S_3$, $S_0 \rightarrow S_4$ and $S_0 \rightarrow S_6$ transitions in the π-stacked D–A–D–A tetramer at the CAM-B3LYP/6-31G(d,p) level of theory

Transition	Wavelength (nm)	Energy (eV)	Oscillator strength	Orbital contribution
$S_0 \rightarrow S_1$	775	1.60	0.202	HOMO−1 → LUMO, 43.86% HOMO → LUMO, 8.11% HOMO → LUMO+1, 48.03%
$S_0 \rightarrow S_3$	639	1.94	0.037	HOMO−1 → LUMO+1, 100%
$S_0 \rightarrow S_5$	432	2.87	0.046	HOMO−2 → LUMO, 4.74% HOMO−2 → LUMO+1, 71.64% HOMO−1 → LUMO+1, 9.93% HOMO → LUMO+2, 13.74%
$S_0 \rightarrow S_6$	420	2.95	0.132	HOMO−11 → LUMO, 2.34% HOMO−3 → LUMO+1, 58.64% HOMO−2 → LUMO, 19.35% HOMO → LUMO+1, 19.77%

integral is computed from the energy splitting between the HOMO orbitals (*i.e.*, HOMO and HOMO−1) of the π-stacked D–A–D trimer. In addition, electron and hole transfer can also take place by direct transfer between the nearest donor or the acceptor molecules.[62–65] The transfer integral values corresponding to direct electron or hole transfer were calculated from the energy splitting of the LUMO of the nearest acceptor dimer and the energy splitting of the HOMO of the nearest donor dimer, respectively.[66] The reorganization energy (λ) term corresponds to the energy requirement due to a change in the geometry of a molecule and its surroundings when it accepts or ejects an electron (*i.e.*, hole formation). The total reorganization energy is the sum of internal (λ_{int}) or external (λ_{ext}) terms. λ_{int} presents the energy required for a change in molecular geometry upon D^+ or A^- formation from a neutral D/A molecule, while the energy required for a change in the geometries of surrounding molecules is expressed by λ_{ext}.[67,68]

The super-exchange electron (t_e^{super}) and hole (t_h^{super}) transfer integral values in the cocrystal are 45 and 48 meV, respectively, indicating ambipolar transport along the mixed π-stack (Fig. 10). We checked the symmetry and energies of the frontier molecular orbitals on perylene and TCNQ to find the origin of ambipolar transport. The HOMO (−4.96 eV) of perylene and the LUMO of TCNQ (−4.81 eV) are energetically close, and both possess vertical ungerade symmetry (Fig. 11a). Hence, the LUMO of the TCNQ molecule acts as a bridging orbital for the super-exchange hole transport from the HOMO of one perylene molecule to the HOMO of another perylene molecule (Fig. 11b). Similarly, the HOMO of the perylene molecule acts as a bridging orbital for electron transport from the LUMO of one TCNQ molecule to the LUMO of a neighbouring TCNQ molecule (Fig. 11b). We showed the importance of the bridging HOMO−1 orbital on the donor in super-exchange mediated electron transport in our previous study.[15] The HOMO−1 orbital of perylene is energetically much lower (−5.75 eV) than the LUMO of TCNQ (Fig. 11a). As a result, this orbital is not supposed to act as a bridging orbital for the super-exchange-mediated electron transport process in the 1:1 perylene:TCNQ cocrystal. The direct hole (t_h^{direct}) and electron (t_e^{direct}) transfer integrals calculated from the nearest D–D and A–A dimers are 8.5 and 7.0 meV, respectively (Fig. S8, SI).

We calculated the internal reorganization energy (λ_{int}) of the perylene and TCNQ moieties from a four-point energy model, as described in Fig. S16. The internal hole reorganization energy of perylene is 147 meV. This small value of λ_{int}

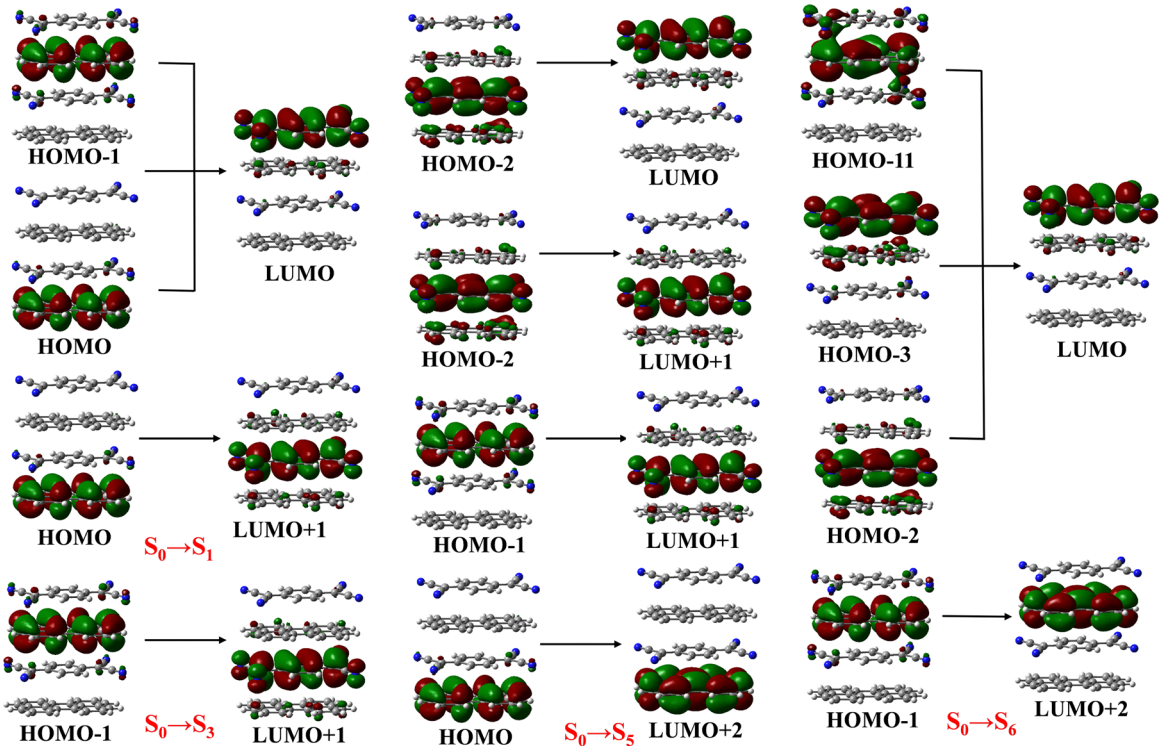

Fig. 8 Molecular orbitals taking part in electronic transitions in the π-stacked D–A–D–A tetramer, where calculations were carried out at the CAM-B3LYP/6-31G(d,p) level of theory.

corresponds with the minimal changes in the respective C–C and C=C bond-lengths from neutral perylene to the perylene radical cation as follows:

C–C and C=C bond-lengths in neutral perylene: 1.430, 1.476, 1.390, 1.375, 1.420, 1.435, and 1.433 Å.

C–C and C=C bond-lengths in perylene cation: 1.452, 1.451, 1.392, 1.390, 1.414, 1.430, and 1.428 Å.

The C≡N, C–C and C=C bond-lengths in the optimized neutral and anionic geometries of TCNQ are listed below. The C≡N bond-lengths in the optimized neutral and anionic geometries of TCNQ are 1.165 and 1.170 Å, respectively. The C–C and C=C bond-lengths in the optimized geometry of TCNQ are 1.427, 1.390, 1.447, 1.355 Å. The C–C and C=C bond-lengths found in the anionic radical geometry of TCNQ are 1.416, 1.432, 1.425, and 1.375 Å (Table S3, SI). The change in bond lengths in TCNQ upon ionization is more prominent than that observed for ionization in perylene, which explains the higher λ_{int} value (255 meV) for TCNQ than perylene.

The internal electron reorganization energy value of TCNQ from our calculation matches well with the value (250 meV) reported in the literature.[69] The comparison of the electron and hole transport rates in the perylene:TCNQ cocrystal was done by considering an activationless transport process,[70] *i.e.*, the free energy of charge carrier transport, $\Delta G^{\neq} = 0$.

As $\Delta G^{\neq} = \Delta G^{\circ} + \lambda = 0$, $\Delta G^{\circ} = -\lambda$ and the rate of charge carrier transfer is as follows:

$$k_T = \frac{4\pi^2}{h}\frac{1}{\sqrt{4\pi\lambda k_B T}}t^2 \text{ as } \exp(0) = 1.$$

The ratio of the hole and electron transfer rates is calculated as $k_T^h/k_T^e = [(48 + 8.5)^2/\sqrt{147}]/[(45 + 7)^2/\sqrt{255}] = 1.55$, considering the super-exchange and direct electron and hole transfer integral values, as well as the internal hole reorganization energy of perylene and the internal electron reorganization energy of TCNQ. This implies that the perylene:TCNQ cocrystal is an ambipolar charge carrier material. It is pertinent to note that the 1 : 1 perylene : TCNQ cocrystal system was deemed as an n-type semiconductor from experimental mobility value measurements in the literature.[41a,c] In contrast, this cocrystal was found to be an ambipolar semiconductor according to DFT calculations by us and others.[41b] We are not sure of the origin of the disparity between the theoretical and experimental results.

We also estimated the internal and external components of the total reorganization energy using the QM/MM model. The unit cell was fully relaxed in both the neutral and charged optimized states, producing the $E^N_{geom=N}$ and $E^C_{geom=C}$ terms of the total reorganization energy. One perylene or one TCNQ molecule was treated in the QM layer and at the B3LYP/6-31G(d,p) level of theory, while the other molecules were treated within the MM layer using the universal force field (UFF) with polarization embedding and charge equilibration (QEq).[71] The terms $E^C_{geom=N}$ and $E^N_{geom=C}$ denote single-point charged total energy carried out at the optimized neutral geometry and single-point neutral total energy carried out at the optimized charged geometries, respectively. The total reorganization energy λ^{tot} (*i.e.*, $\lambda^{int} + \lambda^{ext}$) is calculated following the four-point energy model:[72]

$$\lambda^{tot} = 1/2 \times (E^C_{geom=N} - E^C_{geom=C} + E^N_{geom=C} - E^N_{geom=N}) \quad (5)$$

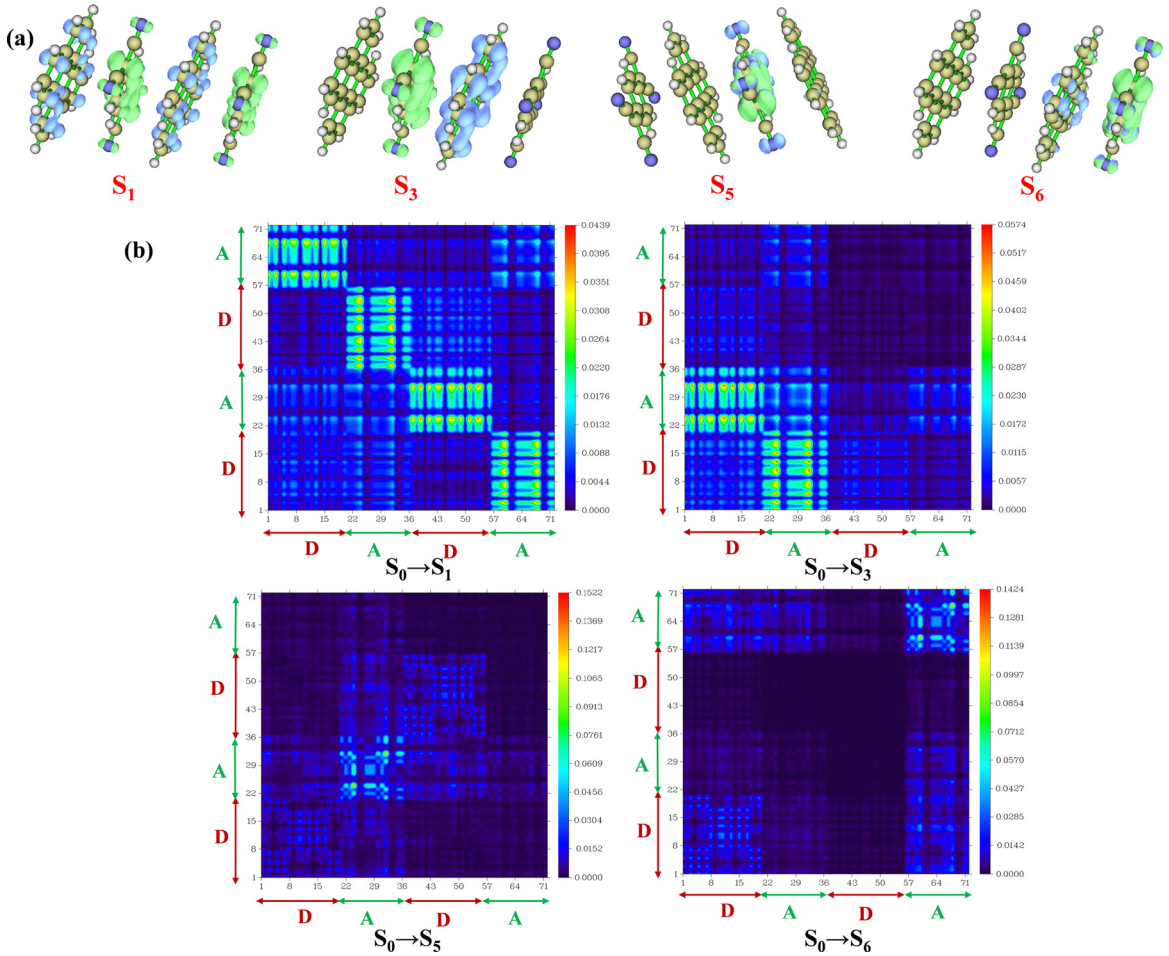

Fig. 9 (a) Electron–hole distribution in the excited states S_1, S_3, S_5 and S_6 calculated at the CAM-B3LYP/6-31G(d,p) level of theory on π-stacked D–A–D–A tetramer and (b) heat maps of one-electron transition density matrix for the $S_0 \rightarrow S_1$, $S_0 \rightarrow S_3$, $S_0 \rightarrow S_5$ and $S_0 \rightarrow S_6$ transitions in the π-stacked D–A–D–A tetramer.

Table 4 Excited-state properties of the π-stacked D–A dimer and D–A–D–A tetramer to understand exciton dynamics, calculated at the CAM-B3LYP/6-31G(d, p) level of theory

System	Excited state	Charge transfer length (Å)	Electron–hole mixing coefficient
D–A dimer	S_1	3.38	0.38
	S_2	2.81	0.42
	S_3	0.49	0.84
A–D–A–D tetramer	S_1	7.67	0.34
	S_3	6.46	0.37
	S_5	0.93	0.82
	S_6	3.28	0.73

The external reorganization energy of the 1 : 1 perylene : TCNQ cocrystal is only 12 meV using the universal force field for the MM region and one TCNQ molecule in the QM region; in contrast, the external reorganization energy is 49.8 meV using universal force field for the MM region and one perylene molecule in the QM layer. These values indicate that the perylene:TCNQ cocrystal has low external reorganization energy, which is favourable for charge carrier transport since thermal energy loss is expected to be small. The difference in the external reorganization energy value when calculated using TCNQ or perylene can be explained by the relative size of these two molecules and their effect in the packed crystal structure. The larger size of the perylene molecule is expected to have a more prominent effect on the neighbouring molecules compared to the effect exerted by the small-sized TCNQ molecule.

Band structure analysis of perylene:TCNQ cocrystal

The band structure of the perylene:TCNQ cocrystal was calculated with both the generalized gradient approximation (GGA) PBE functional and the HSE06 hybrid functional at the experimental unit cell and optimized geometries. The HSE06 hybrid exchange–correlation functional is generally considered to be more accurate for bandgap calculations in comparison to most DFT functionals. However, the HSE06 functional is still reported to underestimate the bandgap value with a mean error of 0.2–0.25 eV.[73]

The band structure is plotted along the high-symmetry points in the first Brillouin zone (Fig. 12a), and the coordinates of the high-symmetry points of the first Brillouin zone are listed

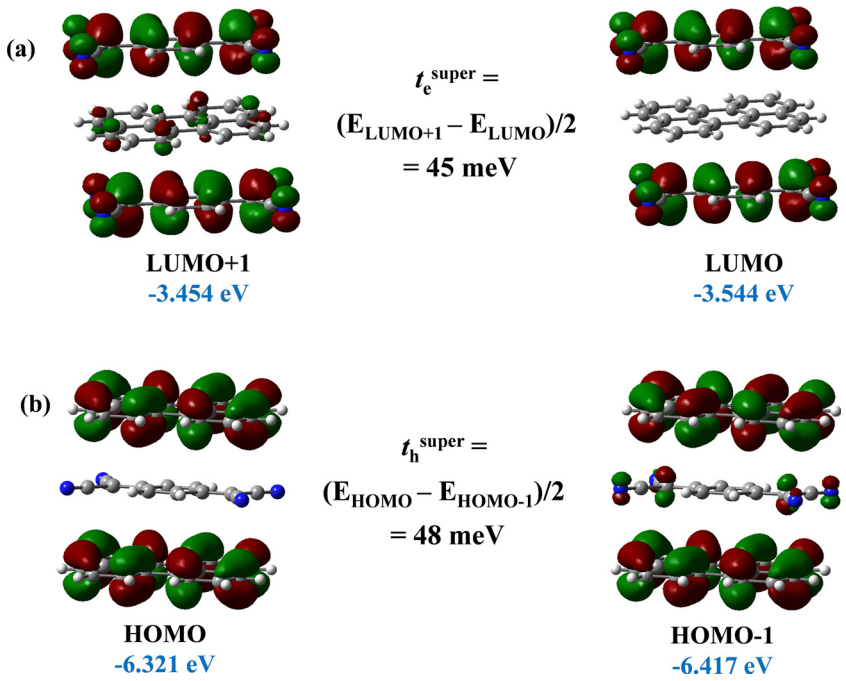

Fig. 10 (a) Super-exchange electron transfer integral calculated for the A–D–A trimer and (b) super-exchange hole transfer calculated for the D–A–D trimer.

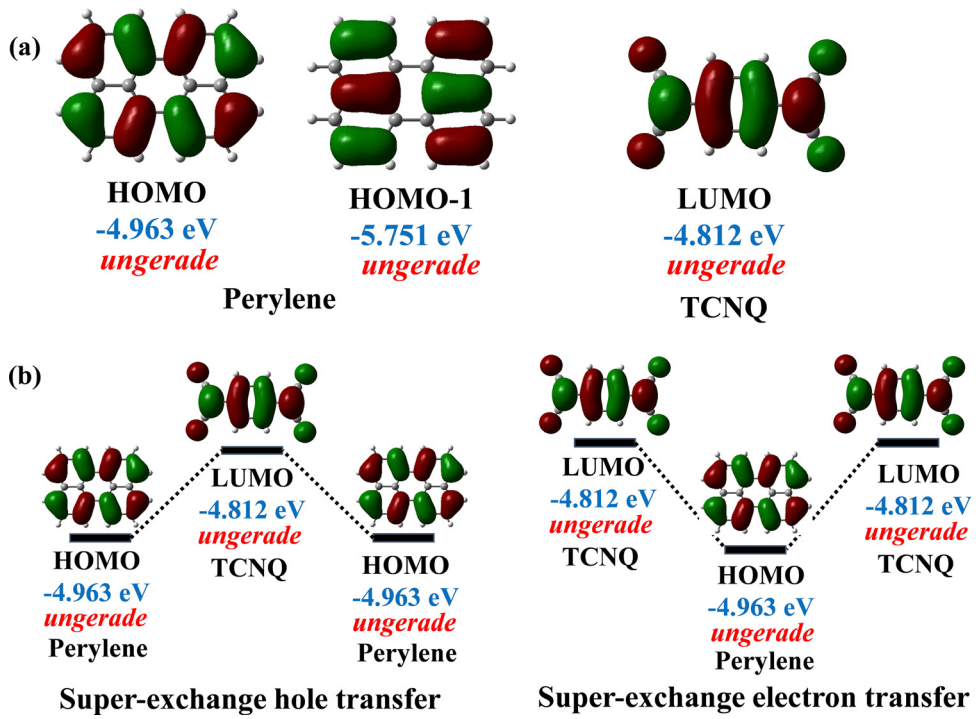

Fig. 11 (a) Energy and symmetry of frontier molecular orbitals on perylene and TCNQ calculated at the B3LYP/6-31G(d,p) level of theory on optimized gas-phase geometries and (b) super-exchange hole and electron transfer processes in the 1 : 1 perylene : TCNQ cocrystal.

in Table S4 in the SI. The perylene : TCNQ cocrystal is an indirect bandgap semiconductor with the valence band maximum residing at the high-symmetry Γ (0, 0, 0) point, while its conduction band minimum (0, 0.25, 0) is not a high-symmetry point (Fig. 12 and Fig. S10 in SI). The calculated bandgap values of the cocrystal using the HSE06 functional on the experimental

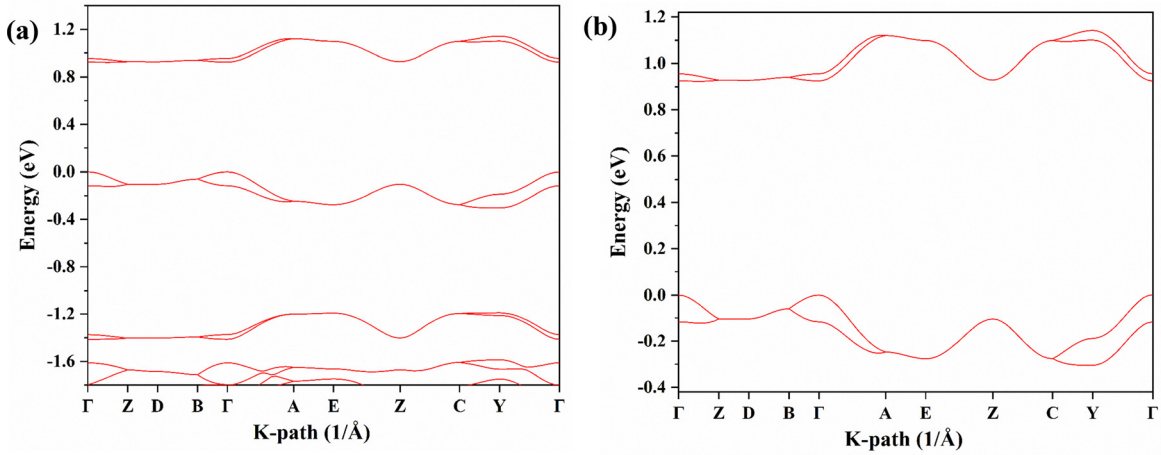

Fig. 12 (a) Band structure of the 1 : 1 perylene : TCNQ cocrystal calculated using the experimental geometry with the HSE06 hybrid functional using a Monkhorst–pack *k*-point mesh of 5 × 3 × 2, an energy cut-off of 500 eV and a Gaussian smearing scheme and (b) bands near VBM and CBM are shown.

and optimized unit geometries are 0.92 and 0.91 eV, respectively. In contrast, the bandgap calculated using the GGA functional PBE is considerably smaller, with a value of only 0.25 eV (Fig. 12b). Two noticeable curvatures are found in the valence and conduction bands, *viz.* along the B (0, 0, 0.5) → A (−0.5, 0, 0.5) direction, indicating the crystallographic *a* axis, and along the E (−0.5, 0.5, 0.5) → C (−0.5, 0.5, 0) direction, indicating the crystallographic *c* axis (Fig. 12). The first one is the direction of π···π stacking between the donor and acceptor, *i.e.*, the direction of super-exchange electron or hole transfer. The second curvature along the crystallographic *c* axis does not indicate any non-covalent interaction bonded chain of donor or acceptor molecules, but rather the close proximity of the neighbouring donor or acceptor molecules along the *c* axis (Fig. 13).

The optical bandgap of the 1 : 1 perylene : TCNQ cocrystal calculated from the Tauc plot is 0.80 eV (Fig. 14a) considering an indirect optical bandgap material according to the following equation:

$$(\alpha h\nu)^{1/2} = h\nu - E_g; \quad (6)$$

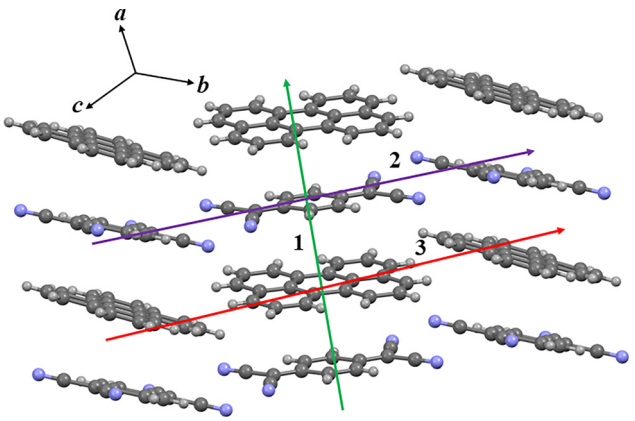

Fig. 13 Different directions of electron and hole transport in the 1 : 1 perylene : TCNQ cocrystal: (**1**) super-exchange electron/hole transfer, (**2**) direct electron transfer, and (**3**) direct hole transfer.

where α is the absorption coefficient and $h\nu$ is the photon energy. The $S_0 \rightarrow S_1$ (E = 1.52 eV), $S_0 \rightarrow S_2$ (E = 2.70 eV), and $S_0 \rightarrow S_3$ (E = 3.20 eV) transitions are clearly observed in the Tauc plot. The oscillator strength of the $S_0 \rightarrow S_1$ transition in the NIR region is relatively small (f = 0.073) compared to the $S_0 \rightarrow S_2$ and $S_0 \rightarrow S_3$ transitions in the visible region; however, it is not negligible, leading to absorption in the NIR region, as can be observed in the Tauc plot. The optical bandgap calculated from the interpolation is 0.80 eV considering an indirect optical bandgap. The exciton binding energy (E_b) of the cocrystal is calculated from the difference between the optical bandgap and the DFT-estimated electronic bandgap. The small exciton binding energy value (0.12 eV) for the perylene:TCNQ cocrystal indicates efficient exciton dissociation and its potential as an organic photovoltaic material.[74] However, this exciton binding energy value might not be fully accurate considering the reported under-estimation of the electronic bandgap by the HSE06 functional. It is pertinent to mention that we also obtained a Tauc plot considering the direct optical bandgap using the following equation''

$$(\alpha h\nu)^2 = h\nu - E_g. \quad (7)$$

The estimated direct optical bandgap is 2.70 eV; however, this bandgap value does not correspond to the absorption features of the cocrystal or to the DFT-calculated electronic bandgap value (Fig. S11, SI).

To understand the potential of the 1 : 1 perylene : TCNQ cocrystal as a photovoltaic material, we calculated the 'spectroscopy limited maximum efficiency' (SLME) parameter proposed by Yu and Zunger from the periodic DFT study.[76] The SLME value was calculated using the VASPKIT optical property evaluation tools.[77] The SLME parameter indicates the maximum theoretical photoconversion efficiency of a material. The cocrystal shows an SLME value of 24% at a thin-film thickness of 1000 nm, which is a remarkable theoretical photoconversion efficiency for an organic semiconductor. This high SLME value

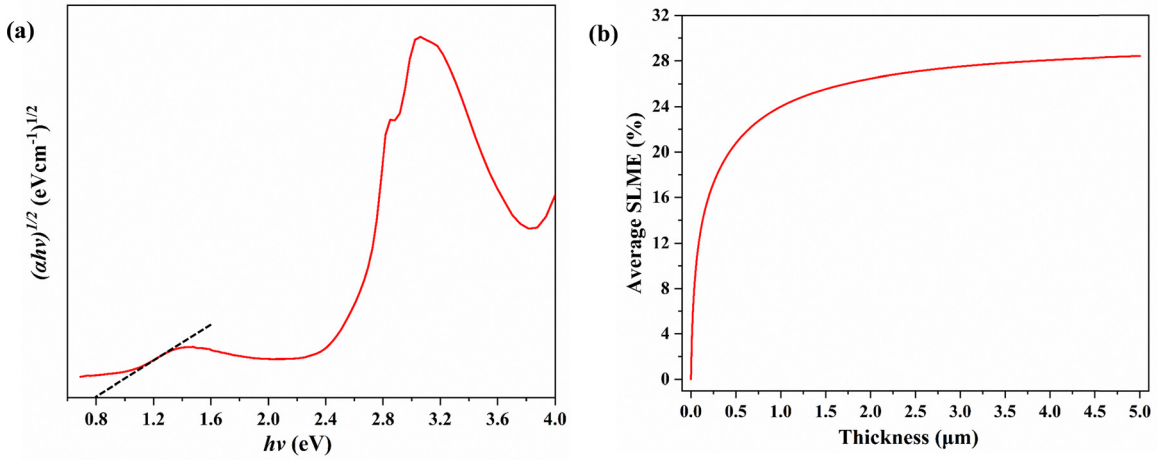

Fig. 14 (a) Tauc plot of the 1 : 1 perylene : TCNQ cocrystal considering an indirect optical bandgap and (b) spectroscopic limited maximal efficiency (SLME) calculated using the experimental unit cell geometry, HSE06 functional, energy cut-off of 500 eV, Gaussian smearing, and Monkhorst–pack k-point mesh of 5 × 3 × 2.

at a lower thin-film thickness is surprising for an indirect bandgap material and is, in part, a direct consequence of the fundamental bandgap (0.92 eV) and the direct allowed bandgap (0.93 eV) being very similar. The high SLME value of the 1 : 1 perylene : TCNQ cocrystal is also attributed to this system absorbing both in the visible and NIR regions. The SLME parameter takes into account the absorption of a material in the standard AM 1.5 G solar spectrum, which spans the range of 280–2000 nm (0.62–4.42 eV). The 1 : 1 perylene : TCNQ system shows absorption spanning from 325–1150 nm (1.08–3.82 eV) and utilizes a wide range of the AM 1.5 G solar spectrum to have high SLME value.

To understand the relation between the band structure features and the SLME values, we investigated the optical properties of two reported semiconductor D–A cocrystals (Fig. S12, SI), *viz.* 1 : 1 1-aminopyrene : TCNQ and 1 : 2 CBP : $(TCNQ)_2$ (CBP is the π-donor 4,4′-bis(carbazol-9-yl)biphenyl) with electron-dominant transport features.[78,79] Both the 1-minopyrene:TCNQ and CBP:$(TCNQ)_2$ cocrystals have an indirect bandgap. The 1-aminopyrene:TCNQ cocrystal shows a spectroscopic limited maximal efficiency value of 23% at a thin-film thickness of 1000 nm, while its fundamental bandgap and direct allowed bandgap values are 0.81 and 0.85 eV, respectively. Similarly, the CBP:$(TCNQ)_2$ cocrystal shows an SLME value 29% at a thin-film thickness of 1000 nm, with the fundamental bandgap and the direct allowed bandgap values of 0.92 and 0.97 eV, respectively. Direct bandgap materials are known for efficient photon absorption even at low thickness, resulting in high SLME values. In contrast, indirect bandgap materials do not absorb photons efficiently at low thickness, resulting in low SLME values. Nevertheless, achieving high SLME values with low thin film thickness is possible for indirect bandgap organic materials if the difference between the fundamental bandgap and the direct allowed bandgap is considerably small, as this will help to minimize the non-radiative recombination pathways.[75] The commercial indirect bandgap semiconductor materials Cs_3AlTe_3 and Cu_3TlS_2 have SLME values of around 25%. The difference between the indirect bandgap and direct allowed bandgap in Cs_3AlTe_3 is 0.07 eV, while it is 0.14 eV for Cu_3TlS_2.[75] The difference between the indirect bandgap and direct allowed bandgap is $\leq$0.05 eV in our studied cocrystals, leading to higher SLME values for these systems.

It is pertinent to mention that the SLME parameter considers photon absorption, exciton generation and dissociation and recombination processes. It is not related to electron and hole transport processes. Electron and hole transport to the electrodes is a major factor deciding the actual photoconversion efficiency. The efficiency of a photovoltaic device depends not only on the optical properties of its constituent materials but also on their charge carrier transport properties and fabrication conditions such as thin-film engineering, electrode materials and dimensions. Hence, the SLME value gives a good estimation of the theoretical maximum photoconversion efficiency, but not the true efficiency of a photovoltaic device. We discussed the electron and hole transport pathways and the corresponding transfer integral values in this study. However, the device fabrication is out of the scope of this theoretical study.

Conclusion

In this work, we elucidated the photophysical and charge carrier transport features of a 1 : 1 cocrystal of a perylene donor and a 7,7′,8,8′-tetracyanoquinodimethane (TCNQ) acceptor with infinite π-stacked chains of alternating donor and acceptor molecules. This cocrystal is characterized by strong charge transfer from the perylene to the TCNQ moiety, which leads to absorption in the far-red and near-infrared regions of the solar spectrum. The electronic bandgap (0.92 eV), the small exciton binding energy value (0.12 eV), and the prominent electron–hole geometric offset in the optical excited states with significant distance between the electron and hole epicenters in the cocrystal suggest efficient photon absorption and exciton

generation and dissociation. The 1 : 1 perylene : TCNQ cocrystal exhibits ambipolar semiconductor behaviour with significant super-exchange electron (45 meV) and hole (48 meV) transfer integral values along the π-stacked ···D–A–D–A··· chains. The low internal hole reorganization energy values of perylene (147 meV) and TCNQ (255 meV) are conducive to fast charge transport and low thermal energy loss; in addition, this system also shows a very low external reorganization energy.

The cocrystal is characterized by an indirect bandgap; however, it still shows a high spectroscopic limited maximal efficiency (SLME) value (24%) at a 1000-nm thin-film thickness suitable for thin-film photovoltaic applications. This intriguing feature of high theoretical photoconversion efficiency is intimately linked with the very similar values of fundamental bandgap and direct allowed bandgap, consequently suppressing the non-radiative recombination pathways. This illustrates that achieving high theoretical photoconversion efficiency at low thin-film thicknesses with indirect bandgap organic semiconductors is possible. This fact was further supported by the calculated SLME values for two reported semiconductor D–A cocrystals, 1-aminopyrene:TCNQ and CBP:$(TCNQ)_2$, with indirect bandgaps. Both cocrystals have very similar fundamental bandgap and direct allowed bandgap values and show SLME values over 20% at a 1000 nm thin film thickness. The current study explores the optoelectronic features of a sustainable D–A cocrystal that can be easily synthesized and solution-processed under ambient conditions, showing promise for implementation in photovoltaic devices. Additionally, this study elucidates how detailed features of the band structures impact the theoretical photoconversion efficiency. Mostly organic semiconductors with direct bandgaps have been studied in detail. Our study first elucidated the scope of organic semiconductors with indirect bandgaps for photovoltaic applications. The D–A organic cocrystal shows great potential as an ambipolar or n-type molecular semiconductor, and this study further reveals its potential as a solution-processable, thin-film photovoltaic material.

Author contributions

AM: conceptualizing the project, performing structural and DFT studies, writing the main draft, acquiring funding; CEM: performing DFT calculations, editing manuscript, acquiring funding; CHG: describing the molecular structure; and YC: acquiring and interpreting the absorption spectrum.

Conflicts of interest

There are no conflicts to declare.

Data availability

The following is the supplementary data related to this article: crystallographic parameters of the perylene:TCNQ cocrystal, and computational details can be obtained in the supplementary information (SI) section of online version of the article. Supplementary information: Table S1: crystallographic and refinement table; Fig. S1: ORTEP diagram of perylene:TCNQ, Fig. S2: formation of perylene:TCNQ; Fig. S3–S6: molecular orbital description of the π-stacked dimer and tetramer, and hexamer in perylene:TCNQ; Table S2 and Fig. S7: time dependent DFT (TD-DFT) calculations on π-stacked dimer in perylene:TCNQ; Table S3: bond-lengths in neutral and anionic TCNQ; S8: direct electron and hole transfer integral in perylene:TCNQ; Fig. S9: calculated absorption spectra by the periodic DFT of perylene:TCNQ; Table S4: coordinates of high symmetry points of perylene:TCNQ; Fig. S10: band structure of perylene:TCNQ calculated using PBE functional; Table S5: coordinates of high symmetry points of 1-aminopyrene:TCNQ and CBP:$(TCNQ)_2$; Fig. S11: fitting Tauc plot for direct bandgap of perylene:TCNQ; Fig. S12: unit cell of 1-aminopyrene:TCNQ and CBP:$(TCNQ)_2$ cocrystals; Fig. S13: band structure, calculated absorption spectrum and SLME of 1-aminopyrene:TCNQ; and Fig. S14: band structure, calculated absorption spectrum and SLME of CBP:$(TCNQ)_2$. See DOI: https://doi.org/10.1039/d6cp00757k.

Acknowledgements

This work has received funding from the European Union's Horizon Europe research and innovation programme under the Marie Skłodowska-Curie grant agreement No. 101106582 and from the Growth House of the University of Oslo grant agreement No. 15300500/102419163. Computational resources were provided by the Norwegian infrastructure for high-performance computing (NOTUR) through a grant of computing time (grant number NN2916K). AM thanks Dr Javier Carmona Garcia from the School of Chemistry, University of Bristol for useful discussions.

References

1 A. W. Hains, Z. Liang, M. A. Woodhouse and B. A. Gregg, Molecular semiconductors in organic photovoltaic cells, *Chem. Rev.*, 2010, **110**(11), 6689–6735.
2 C. M. Aitchison and I. McCulloch, Organic Photovoltaic Materials for Solar Fuel Applications: A Perfect Match?, *Chem. Mater.*, 2024, **36**(4), 1781–1792.
3 W. C. Su, C. C. Lee, Y. Z. Li and S. W. Liu, Influence of Singlet and Charge-Transfer Excitons on the Open-Circuit Voltage of Rubrene/Fullerene Organic Photovoltaic Device, *ACS Appl. Mater. Interfaces*, 2016, **8**, 28757–28762.
4 M. W. B. Wilson, A. Rao, B. Ehrler and R. H. Friend, Singlet Exciton Fission in Polycrystalline Pentacene: From Photophysics toward Devices, *Acc. Chem. Res.*, 2013, **46**(6), 1330–1338.
5 S. D. Oosterhout, V. Savikhin, J. Zhang, Y. Zhang, M. A. Burgers, S. R. Marder, G. C. Bazan and M. F. Toney, Mixing Behavior in Small Molecule:Fullerene Organic Photovoltaics, *Chem. Mater.*, 2017, **29**, 3062–3069.

6 J. Qian, S. Jiang, S. Li, X. Wang, Y. Shi and Y. Li, Solution-Processed 2D Molecular Crystals: Fabrication Techniques, Transistor Applications, and Physics, *Adv. Mater. Technol.*, 2019, **4**, 1800182.
7 A. F. Eftaiha, J. P. Sun, I. G. Hill and G. C. Welch, Recent advances of non-fullerene, small molecular acceptors for solution processed bulk heterojunction solar cells, *J. Mater. Chem. A*, 2014, **2**, 1201–1213.
8 W. Chen and Q. Zhang, Recent progress in non-fullerene small molecule acceptors in organic solar cells (OSCs), *J. Mater. Chem. C*, 2017, **5**, 1275–1302.
9 J. Zhang, H. S. Tan, X. Guo, A. Facchetti and H. Yan, Material insights and challenges for non-fullerene organic solar cells based on small molecular acceptors, *Nat. Energy*, 2018, **3**, 720–731.
10 A. Armin, W. Li, O. J. Sandberg, Z. Xiao, L. Ding, J. Nelson, D. Neher, K. Vandewal, S. Shoaee, T. Wang, H. Ade, T. Heumüller, C. Brabec and P. Meredith, A History and Perspective of Non-Fullerene Electron Acceptors for Organic Solar Cells, *Adv. Energy Mater.*, 2021, **11**, 20003570.
11 M. Kim, S. U. Ryu, S. A. Park, Y. J. Pu and T. Park, Designs and understanding of small molecule-based non-fullerene acceptors for realizing commercially viable organic photovoltaics, *Chem. Sci.*, 2021, **12**, 14004–14023.
12 M. M. Mandoc, F. B. Kooistra, J. C. Hummelen, B. de Boer and P. W. M. Blom, Effect of traps on the performance of bulk heterojunction organic solar cells, *Appl. Phys. Lett.*, 2007, **91**, 263505.
13 S. R. Cowan, N. Banerji, W. L. Leong and A. J. Heeger, Charge Formation, Recombination, and Sweep-Out Dynamics in Organic Solar Cells, *Adv. Funct. Mater.*, 2012, **22**, 1116–1128.
14 H. Zhang, L. Jiang, Y. Zhen, J. Zhang, G. Han, X. Zhang, X. Fu, Y. Yi, W. Xu, H. Dong, W. Chen, W. Hu and D. Zhu, Organic Cocrystal Photovoltaic Behavior: A Model System to Study Charge Recombination of C60 and C70 at the Molecular Level, *Adv. Electron. Mater.*, 2016, **2**, 1500423.
15 A. Mandal, C. E. Mohn, C. H. Görbitz and A. Roy, Cocrystal Engineering of Organic Semiconductors for Photovoltaic Applications: Modeling Excited-State Properties of a Charge Transfer Cocrystal of a Dicarbazole Donor and a Fluoranil Acceptor, *J. Phys. Chem. C*, 2026, **130**(2), 882–897.
16 N. Yee, A. Dadvand and D. F. Perepichka, Band gap engineering of donor–acceptor co-crystals by complementary two-point hydrogen bonding, *Mater. Chem. Front.*, 2020, **4**, 3669–3677.
17 S. Li, L. Zheng, Y. Chan, B. Li, Y. Sun, L. Sun, C. Zhen, X. Zhang and W. Hu, An organic cocrystal based on phthalocyanine with ideal packing mode towards high-performance ambipolar property, *J. Mater. Chem. C*, 2022, **10**, 9596–9601.
18 P. Yu, Y. Li, H. Zhao, L. Zhu, Y. Wang, W. Xu, Y. Zhen, X. Wang, H. Dong, D. Zhu and W. Hu, 1D Mixed-Stack Cocrystals Based on Perylene Diimide toward Ambipolar Charge Transport, *Small*, 2021, **17**, 2006574.
19 W. Wang, L. Luo, Z. Lin, Z. Mu, Z. Ju, B. Yang, Y. Li, M. Lin, G. Long, J. Zhang, J. Zhao and W. Huang, Cocrystal engineering of molecular rearrangement: a ''turn-on'' approach for high-performance N-type organic semiconductors, *J. Mater. Chem. C*, 2021, **9**, 7928–7935.
20 R. Sato, T. Kawamoto and T. Mori, Asymmetrical hole/electron transport in donor–acceptor mixed-stack cocrystals, *J. Mater. Chem. C*, 2019, **7**, 567–577.
21 J. H. Lee, D. H. Lee, H. J. Kim, S. Choi, G. E. Park, M. J. Cho and D. H. Choi, Ambipolar Charge Transport in a Donor–Acceptor–Donor-Type Conjugated Block Copolymer and Its Gate-Voltage-Controlled Thin Film Transistor Memory, *J. Polym. Sci., Part A:Polym. Chem.*, 2017, **55**, 3223–3235.
22 J. Lee, A. R. Han, H. Yu, T. J. Shin, C. Yang and J. H. Oh, Boosting the Ambipolar Performance of Solution-Processable Polymer Semiconductors *via* Hybrid Side-Chain Engineering, *J. Am. Chem. Soc.*, 2013, **135**, 9540–9547.
23 J. Zhang, H. Geng, T. S. Virk, Y. Zhao, J. Tan, C. Di, W. Xu, K. Singh, W. Hu, Z. Shuai, Y. Liu and D. Zhu, Sulfur-Bridged Annulene-TCNQ Co-Crystal: A Self-Assembled ''Molecular Level Heterojunction'' with Air Stable Ambipolar Charge Transport Behavior, *Adv. Mater.*, 2012, **24**, 2603–2607.
24 A. Mandal, A. Choudhury, S. Sau, P. K. Iyer and P. Mal, Exploring Ambipolar Semiconductor Nature of Binary and Ternary Charge-Transfer Cocrystals of Triphenylene, Pyrene, and TCNQ, *J. Phys. Chem. C*, 2020, **124**(12), 6544–6553.
25 W. R. Bodlos, S. K. Park, B. Kunert, S. Y. Park and R. Resel, Thin Film Growth of a Charge Transfer Cocrystal (DCS/TFPA) for Ambipolar Thin Film Transistors, *ACS Appl. Electron. Mater.*, 2021, **3**, 2783–2789.
26 Y. Su, Y. Li, J. Liu, R. Xing and Y. Han, Donor–acceptor cocrystal based on hexakis(alkoxy)triphenylene and perylenediimide derivatives with an ambipolar transporting property, *Nanoscale*, 2015, **7**, 1944–1955.
27 G. Gao, M. Chen, J. Roberts, M. Feng, C. Xiao, G. Zhang, S. Parkin, C. Risko and L. Zhang, Rational Functionalization of a C70 Buckybowl To Enable a C70:Buckybowl Cocrystal for Organic Semiconductor Applications, *J. Am. Chem. Soc.*, 2020, **142**(5), 2460–2470.
28 W. Sun, Y. Zheng, K. Yang, Q. Zhang, A. A. Shah, Z. Wu, Y. Sun, L. Feng, D. Chen, Z. Xiao, S. Lu, Y. Li and K. Sun, Machine learning–assisted molecular design and efficiency prediction for high-performance organic photovoltaic materials, *Sci. Adv.*, 2019, **5**, eaay4275.
29 J. Roncali, P. Leriche and P. Blanchard, Molecular Materials for Organic Photovoltaics: Small is Beautiful, *Adv. Mater.*, 2014, **26**, 3821–3838.
30 T. Salzillo, M. Masino, G. K. Köhn, D. D. Nuzzo, E. Venuti, R. G. D. Valle, D. Vanossi, C. Fontanesi, A. Girlando, A. Brillante and E. D. Como, Structure, Stoichiometry, and Charge Transfer in Cocrystals of Perylene with TCNQ-Fx, *Cryst. Growth Des.*, 2016, **16**, 3028–3036.
31 T. Salzillo, R. G. Della Valle, E. Venuti, G. K. Köhn, M. Masino, A. Girlando and A. Brillante, Solution equilibrium between two structures of Perylene-F_2TCNQ charge transfer co-crystals, *J. Cryst. Growth*, 2019, **516**, 45–50.
32 J. Guo, L. Xu, M. Cai, Z. Dong, Q. Mu, X. Wang, H. Fan, F. Teng, X. He, H. Jiang and P. Hu, Crystal Growth,

Intermolecular Noncovalent Interactions, and Photoluminescence Properties of Halogenated Phthalic Anhydride-Based Organic Charge Transfer Cocrystals, *Cryst. Growth Des.*, 2024, **24**, 1293–1301.

33 J. Zhang, J. Chen, B. Yang, S. Ma, L. Yin, Z. Liu, W. Xiang, H. Liu, J. Zhao and P. Sheng, Energy Level, Crystal Morphology and Fluorescence Emission Tuning in Cocrystals via Molecular-Level Engineering, *Chem. – Eur. J.*, 2023, **29**, e202202915.

34 J. Li, S. Takaishi, N. Fujinuma, K. Endo, M. Yamashita, H. Matsuzaki, H. Okamoto, K. Sawabe, T. Takenobu and Y. Iwasa, Enhancement of luminescence intensity in TMPY/perylene co-single crystals, *J. Mater. Chem.*, 2011, **21**, 17662–17666.

35 A. Ashokan, C. Hanson, N. Corbin, J. L. Brédas and V. Coropceanu, Electronic, vibrational, and charge-transport properties of benzothienobenzothiophene-TCNQ co-crystals, *Mater. Chem. Front.*, 2020, **4**, 3623–3631.

36 Q. Ai, Y. A. Getmanenko, K. Jarolimek, R. Castañeda, T. V. Timofeeva and C. Risko, Unusual Electronic Structure of the Donor−Acceptor Cocrystal Formed by Dithieno[3,2-a:2′,3′-c]phenazine and 7,7,8,8-Tetracyanoquinodimethane, *J. Phys. Chem. Lett.*, 2017, **8**, 4510–4515.

37 S. Melis, S. Hung, C. Bagade, Y. Chung, E. Hughes, X. Zhang, P. Barbara, P. Han, T. Li, D. McCusker, R. Hartsmith, J. Bertke, P. Dev, I. Stone, J. Joshi, P. Vora and E. V. Keuren, Charge Transport through Superexchange in Phenothiazine−7,7,8,8-Tetracyanoquinodimethane (PTZ−TCNQ) Cocrystal Microribbon FETs Grown Using Evaporative Alignment, *ACS Appl. Electron. Mater.*, 2022, **4**(12), 5973–5983.

38 R. Ramanathan, L. L. Martin, A. M. Bond and V. Bansal, Emerging Applications of TCNQ-Based Metal–Organic Semiconducting Materials, *ACS Appl. Nano Mater.*, 2024, **7**(24), 28057–28073.

39 C. Schneider, D. Ukaj, R. Koerver, A. A. Talin, G. Kieslich, S. P. Pujari, H. Zuilhof, J. Janek, M. D. Allendorf and R. A. Fischer, High electrical conductivity and high porosity in a Guest@MOF material: evidence of TCNQ ordering within Cu_3BTC_2 micropores, *Chem. Sci.*, 2018, **9**, 7405–7412.

40 (*a*) I. J. Tickle and C. K. Prout, Molecular Complexes. Part XVII[1] Crystal and Molecular Structure of Perylene-7,7,8,8-Tetracyanoquinodimethane Molecular Complex, *J. Chem. Soc., Perkin Trans. 2*, 1973, 720–723; (*b*) J. Henderson, M. Masino, L. E. Hatcher, G. Kociok-Köhn, T. Salzillo, A. Brillante, P. R. Raithby, A. Girlando and E. D. Como, New Polymorphs of Perylene:Tetracyanoquinodimethane Charge Transfer Cocrystals, *Cryst. Growth Des.*, 2018, **18**, 2003–2009.

41 (*a*) R. Sanada, D. Yoo, R. Sato, K. Iijima, T. Kawamoto and T. Mori, Ambipolar Transistor Properties of Charge-Transfer Complexes Containing Perylene and Dicyanoquinonediimines, *J. Phys. Chem. C*, 2019, **123**, 12088–12095; (*b*) D. Vermeulen, L. Y. Zhu, K. P. Goetz, P. Hu, H. Jiang, C. S. Day, O. D. Jurchescu, V. Coropceanu, C. Kloc and L. E. McNeil, Charge Transport Properties of Perylene−TCNQ Crystals: The Effect of Stoichiometry, *J. Phys. Chem. C*, 2014, **118**, 24688–24696; (*c*) H. D. Wu, H. D. Peng and G. B. Pan, Precise growth of low-dimensional pyrene·perylene·TCNQ co-crystals and structure–property related optoelectronic properties, *RSC Adv.*, 2016, **6**, 78979–78983.

42 S. F. Boys and F. Bernardi, The calculation of small molecular interactions by the differences of separate total energies. Some procedures with reduced errors, *Mol. Phys.*, 1970, **19**, 553–566.

43 C. F. Mackenzie, P. R. Spackman, D. Jayatilaka and M. A. Spackman, *CrystalExplorer* model energies and energy frameworks: extension to metal coordination compounds, organic salts, solvates and open-shell systems, *IUCrJ*, 2017, **4**, 575–587.

44 P. R. Spackman, M. J. Turner, J. J. McKinnon, S. K. Wolff, D. J. Grimwood, D. Jayatilaka and M. A. Spackman, *J. Appl. Crystallogr.*, 2021, **54**, 1006–1011.

45 S. Grimme, Density functional theory with London dispersion corrections, *Wiley Interdiscip. Rev.:Comput. Mol. Sci.*, 2011, **1**, 211–228.

46 S. Grimme, S. Ehrlich and L. Goerigk, Effect of the damping function in dispersion corrected density functional theory, *Comput. Chem.*, 2011, **32**, 1456–1465.

47 F. Weinhold, C. R. Landis and E. D. Glendening, What is NBO analysis and how is it useful?, *Int. Rev. Phys. Chem.*, 2016, **35**, 399–440.

48 A. E. Reed, L. A. Curtiss and F. Weinhold, Intermolecular Interactions from a Natural Bond Orbital, Donor-Acceptor Viewpoint, *Chem. Rev.*, 1988, **88**, 899–926.

49 K. Okuno, Y. Shigeta, R. Kishi and M. Nakano, Non-empirical tuning of CAM-B3LYP functional in time-dependent density functional theory for excitation energies of diarylethene derivatives, *Chem. Phys. Lett.*, 2013, **585**, 201–206.

50 M. Li, J. R. Reimers, M. J. Ford, R. Kobayashi and R. D. Amos, Accurate prediction of the properties of materials using the CAM-B3LYP density functional, *J. Comput. Chem.*, 2021, **42**, 1486–1497.

51 T. Lu, A comprehensive electron wavefunction analysis toolbox for chemists, Multiwfn, *J. Chem. Phys.*, 2024, **161**, 082503.

52 T. Lu and F. Chen, Multiwfn: A multifunctional wavefunction analyzer, *J. Comput. Chem.*, 2012, **33**, 580–592.

53 Y. Li and C. A. Ullrich, Time-dependent transition density matrix, *Chem. Phys.*, 2011, **391**, 157–163.

54 C. H. Moore, P. Jena and J. T. McLeskey Jr, Tuning range-separated DFT functionals for modeling the peak absorption of MEH-PPV polymer in various solvents, *Comput. Theor. Chem.*, 2019, **1162**, 112506.

55 O. L. Estrada, H. G. Laguna, C. B. Flores and C. A. Bedolla, Reassessment of the Four-Point Approach to the Electron-Transfer Marcus−Hush Theory, *ACS Omega*, 2018, **3**, 2130–2140.

56 A. V. Krukau, O. A. Vydrov, A. F. Izmaylov and G. E. Scuseria, Influence of the exchange screening parameter on the performance of screened hybrid functionals, *J. Chem. Phys.*, 2006, **125**, 224106.

57 S. Adhikari, J. Clary, R. Sundararaman, C. Musgrave, D. V. Fowler and C. Sutton, Accurate Prediction of HSE06 Band Structures for a Diverse Set of Materials Using Δ-Learning, *Chem. Mater.*, 2023, **35**(20), 8397–8405.

58 K. Choudhary, M. Bercx, J. Jiang, R. Pachter, D. Lamoen and F. Tavazza, Accelerated Discovery of Efficient Solar Cell Materials Using Quantum and Machine-Learning Methods, *Chem. Mater.*, 2019, **31**, 5900–5908.

59 M. D. Shavez and A. N. Panda, Assessing Effects of Different π bridges on Properties of Random Benzodithiophene-thienothiophene Donor and Non-fullerene Acceptor Based Active Layer, *J. Phys. Chem. A*, 2021, **125**, 9852–9864.

60 S. Kraner, R. Scholz, F. Plasser, C. Koerner and K. Leo, Exciton size and binding energy limitations in one-dimensional organic materials, *J. Chem. Phys.*, 2015, **143**, 244905.

61 R. A. Marcus, Tutorial on rate constants and reorganization energies, *J. Electroanal. Chem.*, 2000, **483**, 2–6.

62 L. Zhu, Y. Yi, Y. Li, E.-G. Kim, V. Coropceanu and J.-L. Brédas, Prediction of remarkable ambipolar charge-transport characteristics in organic mixed-stack charge-transfer crystals, *J. Am. Chem. Soc.*, 2012, **134**, 2340–2347.

63 B. Liu, S. Fan, R. Huang, T. Kawamoto and T. Mori, Transistor Properties of Charge-Transfer Complexes–Combined Requirements from Energy Levels and Orbital Symmetry, *J. Phys. Chem. C*, 2023, **127**, 5125–5133.

64 K. Iijima, R. Sanada, D. Yoo, R. Sato, T. Kawamoto and T. Mori, Carrier charge polarity in mixed-stack charge-transfer crystals containing dithienobenzodithiophene, *ACS Appl. Mater. Interfaces*, 2018, **10**(12), 10262–10269.

65 J. Zhang, W. Xu, P. Sheng, G. Zhao and D. Zhu, Organic Donor−Acceptor Complexes as Novel Organic Semiconductors, *Acc. Chem. Res.*, 2017, **50**, 1654–1662.

66 K. Senthilkumar, F. C. Grozema, F. M. Bickelhaupt and L. D. A. Siebbeles, Charge transport in columnar stacked triphenylenes: Effects of conformational fluctuations on charge transfer integrals and site energies, *J. Chem. Phys.*, 2003, **119**, 9809–9817.

67 N. Metri, X. Sallenave, C. Plesse, L. Beouch, P. H. Aubert, F. Goubard, C. Chevrot and G. Sini, Processable star-shaped molecules with triphenylamine core as hole-transporting materials: Experimental and theoretical approach, *J. Phys. Chem. C*, 2012, **116**(5), 3765–3772.

68 M. E. Köse and K. S. Schanze, Prediction of internal reorganization energy in photoinduced electron transfer processes of molecular dyads, *J. Phys. Chem. A*, 2020, **124**(45), 9478–9486.

69 A. Y. Sosorev, Role of intermolecular charge delocalization and its dimensionality in efficient band-like electron transport in crystalline 2,5-difluoro-7,7,8,8-tetracyanoquinodimethane (F2-TCNQ), *Phys. Chem. Chem. Phys.*, 2017, **19**, 25478–25486.

70 T. P. Silverstein, Marcus Theory: Thermodynamics CAN Control the Kinetics of Electron Transfer Reactions, *J. Chem. Educ.*, 2012, **89**, 1159–1167.

71 A. K. Rappe, C. J. Casewit, K. S. Colwell, W. A. Goddard III and W. M. Skiff, UFF, a full periodic table force field for molecular mechanics and molecular dynamics simulations, *J. Am. Chem. Soc.*, 1992, **114**(25), 10024–10035.

72 D. P. McMahon and A. Troisi, Evaluation of the External Reorganization Energy of Polyacenes, *J. Phys. Chem. Lett.*, 2010, **1**, 941–946.

73 (*a*) A. J. Garza and G. E. Scuseria, Predicting Band Gaps with Hybrid Density Functionals, *J. Phys. Chem. Lett.*, 2016, **7**(20), 4165–4170; (*b*) C. E. Mohn, H. Fjellvåg, P. Vajeeston, M. Valldor and K. Bergum, Benchmarking Density Functional Theory for Accurate Calculation of Nitride Band Gaps, *J. Chem. Theory Comput.*, 2026, **22**, 1321–1337.

74 L. Zhu, J. Zhang, Y. Guo, C. Yang, Y. Yi and Z. Wei, Small Exciton Binding Energies Enabling Direct Charge Photogeneration Towards Low-Driving-Force Organic Solar Cells, *Angew. Chem., Int. Ed.*, 2021, **60**, 15348–15353.

75 A. Sugie, K. Nakano, K. Tajima, I. Osaka and H. Yoshida, Dependence of Exciton Binding Energy on Bandgap of Organic Semiconductors, *J. Phys. Chem. Lett.*, 2023, **14**(50), 11412–11420.

76 L. Yu and A. Zunger, Identification of Potential Photovoltaic Absorbers Based on First-Principles Spectroscopic Screening of Materials, *Phys. Rev. Lett.*, 2012, **108**, 068701.

77 V. Wang, N. Xu, J.-C. Liu, G. Tang and W.-T. Geng, VASPKIT: A User-friendly Interface Facilitating High-throughput Computing and Analysis Using VASP Code, *Comput. Phys. Commun.*, 2021, **267**, 108033.

78 A. Mandal, Tuning p-type to n-type semiconductor nature by charge transfer cocrystallization: effect of transfer integral vs. reorganization energy, *CrystEngComm*, 2022, **24**, 2072–2080.

79 A. Mandal, A. Choudhury, R. Kumar, P. K. Iyer and P. Mal, Exploring the semiconductor properties of a charge transfer cocrystal of 1-aminopyrene and TCNQ, *CrystEngComm*, 2020, **22**, 720–727.